TU Delft

Delft University of Technology

Document Version
Final published version

Licence
Dutch Copyright Act (Article 25fa)

Citation (APA)
Je, Y., Jeong, H., Caneva, S., Steeneken, P. G., Campbell, E. E. B., Lee, S. W., & Shin, D. H. (2026). Strain Field Modulation in Suspended Graphene Membranes Using Localized Electron-Beam-Induced Deposition. *ACS Applied Materials and Interfaces*, *18*(20), 29208-29217. https://doi.org/10.1021/acsami.5c25657

Important note
To cite this publication, please use the final published version (if applicable).
Please check the document version above.

Copyright
In case the licence states “Dutch Copyright Act (Article 25fa)”, this publication was made available Green Open Access via the TU Delft Institutional Repository pursuant to Dutch Copyright Act (Article 25fa, the Taverne amendment). This provision does not affect copyright ownership.
Unless copyright is transferred by contract or statute, it remains with the copyright holder.

Sharing and reuse
Other than for strictly personal use, it is not permitted to download, forward or distribute the text or part of it, without the consent of the author(s) and/or copyright holder(s), unless the work is under an open content license such as Creative Commons.

Takedown policy
Please contact us and provide details if you believe this document breaches copyrights.
We will remove access to the work immediately and investigate your claim.

This work is downloaded from Delft University of Technology.

ACS APPLIED MATERIALS & INTERFACES

www.acsami.org

Research Article

Strain Field Modulation in Suspended Graphene Membranes Using Localized Electron-Beam-Induced Deposition

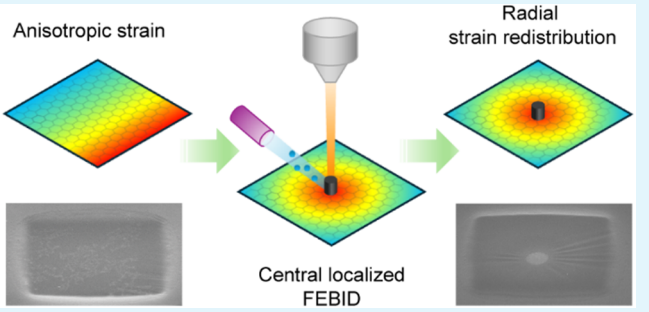
Yugyeong Je,[#] Hyunjeong Jeong,[#] Sabina Caneva, Peter G. Steeneken, Eleanor E. B. Campbell, Sang Wook Lee,* and Dong Hoon Shin*

Cite This: *ACS Appl. Mater. Interfaces* 2026, 18, 29208–29217

Read Online

ACCESS | Metrics & More | Article Recommendations | Supporting Information

ABSTRACT: In atomically thin membranes, strain couples strongly to electrons, phonons, and photons. Although strain originating from uniform or global deformation has been widely studied, the impact of spatially localized mechanical perturbations on strain distribution remains less explored. Here, we investigate how localized tungsten carbide deposition via focused electron-beam-induced deposition (FEBID) modifies the strain landscape in suspended monolayer graphene membranes. Using spatially resolved mechanical resonance mode shape mapping and Raman spectroscopy, supported by finite element simulations, we find that the central deposit acts as a mechanically coupled local perturbation that redistributes the pre-existing strain into a more radially symmetric configuration with reduced angular anisotropy around the deposit. These findings demonstrate that FEBID-based local deposition can serve as a lithography-free approach for controlled strain modulation in suspended graphene, offering a practical platform for studying strain-coupled phenomena and designing strain-controlled nanoelectromechanical and optoelectronic systems.



KEYWORDS: *2D materials, graphene, strain, mechanical resonance mode, Raman spectroscopy, NEMS*

Downloaded via TU DELFT on June 10, 2026 at 12:24:14 (UTC).
See https://pubs.acs.org/sharingguidelines for options on how to legitimately share published articles.

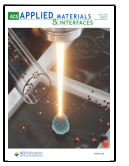
INTRODUCTION

Strain is a powerful tool for tuning the electrical, mechanical, and optical responses of atomically thin crystals, unlocking properties inaccessible in their relaxed state.[1−4] In two-dimensional (2D) materials, controlling not only the average strain but also the spatial distribution of the strain matrix is critical, because electronic structure, vibrational dynamics, and light-matter interactions couple to local symmetry and boundary conditions. Over the past decade, however, most strain studies have relied on globally applied, near-uniform deformations, such as electrostatic gating,[5−7] substrate bending,[5,8−10] thermal mismatch,[11,12] and polymer-assisted techniques.[13−15] Although these approaches offer experimental simplicity, they provide only coarse control and often introduce undesirable strain gradients or time-dependent drift.

Realizing advanced strain-enabled functionalities in 2D materials, such as tunable bandgaps[1,3,15,16] and pseudomagnetic fields,[17,18] demands methods capable of delivering strain with both high spatial resolution and quantitative precision. Toward this goal, three primary approaches have been used for localizing strain. The first is bubble formation, where trapped gas or contaminants between a 2D material and its substrate produce dome-like deformations with symmetric, isotropic strain fields.[19−21] The second is nanoindentation, where a sharp probe induces localized, controllable deformation, enabling systematic investigation of strain-dependent mechanical and electronic properties.[22,23] The third approach relies on strain transfer from nonplanar or topographically patterned substrates, such as nanopillar arrays, corrugated or wrinkled surfaces, where conformal adhesion of the 2D material to the underlying geometry produces spatially modulated strain fields.[24−27] However, all three methods face practical limitations: bubble sizes and positions are hard to reproduce and integrate into devices, whereas nanoindentation can only be applied one point at a time and is not well suited for creating patterned arrays. Lastly, in patterned-substrate approaches, the strain profile is largely governed by the substrate geometry and the degree of conformal contact, which limits postfabrication tunability and requires careful control of transfer and adhesion to minimize local damage or defect formation.

Here, we explore a complementary approach to strain engineering in suspended single-layer graphene (SLG) membranes by locally depositing a nanoscale feature via focused electron-beam-induced deposition (FEBID). Unlike

Received: December 19, 2025
Revised: March 16, 2026
Accepted: May 2, 2026
Published: May 13, 2026



© 2026 American Chemical Society

https://doi.org/10.1021/acsami.5c25657
ACS Appl. Mater. Interfaces 2026, 18, 29208−29217

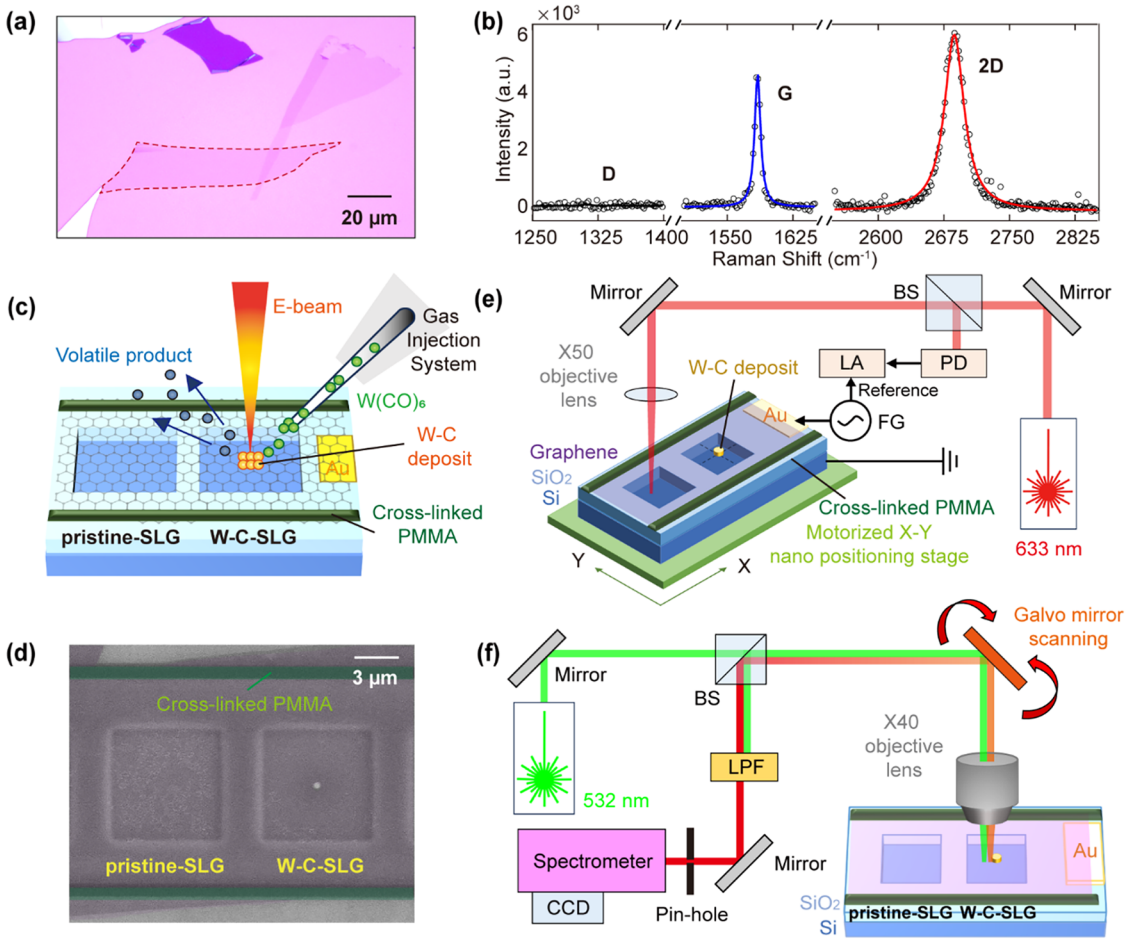


Figure 1. Monolayer graphene square drum and scanning optical interferometry system. (a) Optical image of the exfoliated graphene on SiO_2/Si substrate before transfer on trench substrate. The graphene flake outlined by the dashed red line was used for device fabrication. (b) Raman spectra of the G and 2D bands fitted with Lorentzian functions, showing the unstrained reference frequencies ω_G^0 and ω_{2D}^0. The reference ω_G^0 and ω_{2D}^0 are taken as 1584.67 cm^{-1} and 2686.91 cm^{-1}. (c) Schematic illustration of the FEBID process on a suspended graphene drum, using a tungsten carbonyl $W(CO)_6$ precursor. (d) Scanning electron microscopy (SEM) image of the graphene square drum resonators: pristine-SLG and W−C−SLG drums. Both drums were clamped with cross-linked PMMA bars to stabilize the suspended membranes. (e) Schematic of graphene drum resonator and scanning optical interferometry measurement system using 633 nm excitation laser. (BS: beam splitter, PD: photodetector, LA: lock-in amplifier, FG: function generator). (f) Schematic of the spatially resolved Raman mapping system using a 532 nm excitation laser. (BS: beam splitter, LPF: long-pass edge filter).

bubble-based loading or nanoindentation, which are often transient or loading-dependent, and unlike patterned substrates, where the strain profile is defined by the underlying geometry, FEBID enables site-selective postfabrication modification of a suspended membrane through direct local deposition. Using a combination of dynamic and static measurements, we identify the experimental signatures of the FEBID-induced modulation of the membrane mechanics: resonance-mode imaging resolves the dynamic response,[28,29] spatial Raman mapping quantifies the static strain field, and finite element simulations provide a consistent framework for understanding the underlying mechanism. These measurements show that a deposited feature acts as a mechanically coupled local perturbation that redistributes the transfer-induced spatially nonuniform pretension, leading to a more radially symmetric strain distribution across the suspended graphene, beyond the effect of mass loading. The absence of substrate coupling ensures that the observed strain redistribution directly reflects the intrinsic membrane mechanics. Overall, our results demonstrate that local mechanical modification with layout-compatible FEBID features can reshape the strain landscape in suspended graphene, offering a practical route toward strain-driven functionality.

RESULTS AND DISCUSSION

Comparative Platform Preparation and Baseline Characterization

To investigate the strain response of suspended atomically thin membranes under localized W−C deposition, we designed a comparative experimental platform consisting of two adjacent square cavities. Mechanically exfoliated monolayer graphene (Figure 1a) was transferred onto the prefabricated square cavities, each with a side length of 7 μm and a depth of 280 nm, using a Poly(methyl methacrylate) (PMMA)-assisted wet-transfer method, enabling side-by-side comparison between two suspended graphene membranes and minimizing device-to-device variability. Raman spectra measured before the wet-transfer of supported graphene on a SiO_2/Si substrate, specifically before coating with PMMA, were determined as the pretransfer reference frequencies, with the G-peak position (ω_G^0) and the 2D-peak position (ω_{2D}^0) taken as 1584.67 cm^{-1}

https://doi.org/10.1021/acsami.5c25657
ACS Appl. Mater. Interfaces 2026, 18, 29208−29217

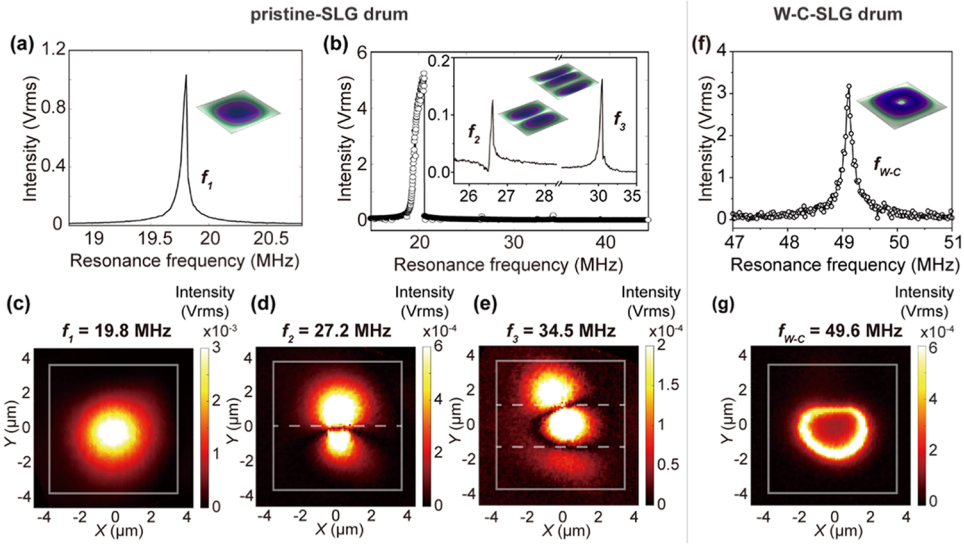


Figure 2. Mechanical resonance frequency and mode observation of (a–e) pristine-SLG drum and (f, g) W–C–SLG drum. (a) Resonance frequency f_1 of a pristine-SLG drum. The applied AC bias is 0.1 V. Insets show simulated mode shape for each mode. (b) Resonance spectrum measured under a driving AC bias of 1.0 V, revealing second and third modes, with simulated mode shapes, corresponding to Panel c, shown as insets. (c) Experimental vibrational mode shape of f_1 in pristine-SLG drum measured by scanning a laser across the surface of the drum with a step size of 100 nm while it was driven at a resonant frequency of 19.8 MHz. (d) Experimental vibrational mode shape of f_2 (27.2 MHz) in pristine-SLG drum. (e) Experimental vibrational mode shape of f_3 (34.5 MHz) in pristine-SLG drum. (f) Resonance frequency of the W–C–SLG drum. The applied AC bias is 0.1 V. Insets show simulated mode shape. (g) Experimental vibrational mode shape in W–C–SLG drum with a step size of 100 nm while it was driven at a resonant frequency (f_{W-C}) of 49.6 MHz.

and 2686.91 cm^{-1}, respectively (Figure 1b). We note that this reference does not represent an absolute zero-strain state. Rather, it serves as a practical experimental baseline for evaluating relative frequency changes upon suspension and subsequent deposition.

After the transfer process, one drum was kept unmodified (pristine-SLG drum), while the other (W–C–SLG drum) was locally loaded with a W–C nanostructure at the center of the drum via FEBID using a $W(CO)_6$ precursor, as schematically illustrated in Figure 1c. We employed FEBID as a direct-write and mask-free technique that offers submicrometer placement accuracy and is compatible with array-level patterning and device integration. The FEBID process was performed under conditions optimized to avoid rupture of the suspended graphene. Prior to FEBID, both drums were clamped using cross-linked PMMA bars formed by high electron-beam dose exposure to stabilize the suspended membranes (Figure 1d). The W–C deposit was designed to have a cylindrical shape, with a diameter of 0.4 μm and a thickness of 1 μm. The calculated mass of the W–C deposit, assuming a composition of 37% tungsten based on the reported result by Mulders et al.[30] and Rosenberg et al.,[31] is about 1.2 pg, which is approximately 32 times the mass of the suspended area of the monolayer graphene drum, ~37 fg. To probe the resulting strain distribution under both static and dynamic conditions, we performed mechanical resonance mode imaging (Figure 1e) and spatially resolved Raman mapping (Figure 1f). Details of the device fabrication, FEBID conditions, and measurement procedures are provided in the Methods section.

Dynamic Behavior Probed by Mechanical Resonance

The vibrational response of the pristine-SLG drum was investigated by applying AC driving voltages between the graphene and the Si substrate to probe the mechanical characteristics encoded in its resonance modes. To avoid introducing a static electrostatic load that could modify the intrinsic mechanical properties of the drum, no external DC gate bias was applied. Despite the absence of an applied DC component, a finite response at the drive frequency is still observed, which we attribute to a small effective DC offset originating from built-in potential due to work-function differences and residual charge in the device circuitry.[32−34] Under an AC driving bias of 0.1 V, the pristine-SLG drum exhibits the fundamental resonance mode (f_1) at 19.8 MHz (Figure 2a). Increasing the driving amplitude to 1.0 V enables the detection of higher-order modes: f_2 at 27.2 MHz and f_3 at 34.5 MHz (Figure 2b). The experimentally measured resonance mode shapes corresponding to these three frequencies f_1–f_3 are shown in Figure 2c–e, respectively.

Finite element simulations using the structural mechanics module in COMSOL Multiphysics were performed to reproduce the experimentally observed resonance mode shapes of the pristine drum. The results confirm that the resonance behavior reflects anisotropic in-plane stress, where the tensile stress along the *x*-direction is greater than that along the *y*-direction. In this stress configuration, out-of-plane deformation is more constrained along the *x*-axis, therefore vibrational modes that contain nodal lines along this direction are pushed to higher frequencies, leading to an increased number of nodal lines along the *y*-axis in higher-order modes. The simulated mode shapes under this anisotropic stress condition are in good agreement with the experimental data (The insets of Figure 2a,2b).

A similar asymmetric mode behavior was also observed in a pristine bilayer graphene (pristine-BLG) drum (Figures S1 and S2). In both monolayer and bilayer devices, the anisotropic in-plane stress is likely induced during the 2D material transfer process, which can introduce residual or uneven stresses into suspended membranes.

We next examined how a localized central deposit alters the resonance behavior. In the W–C–SLG drum, the exper-

https://doi.org/10.1021/acsami.5c25657
ACS Appl. Mater. Interfaces 2026, 18, 29208−29217

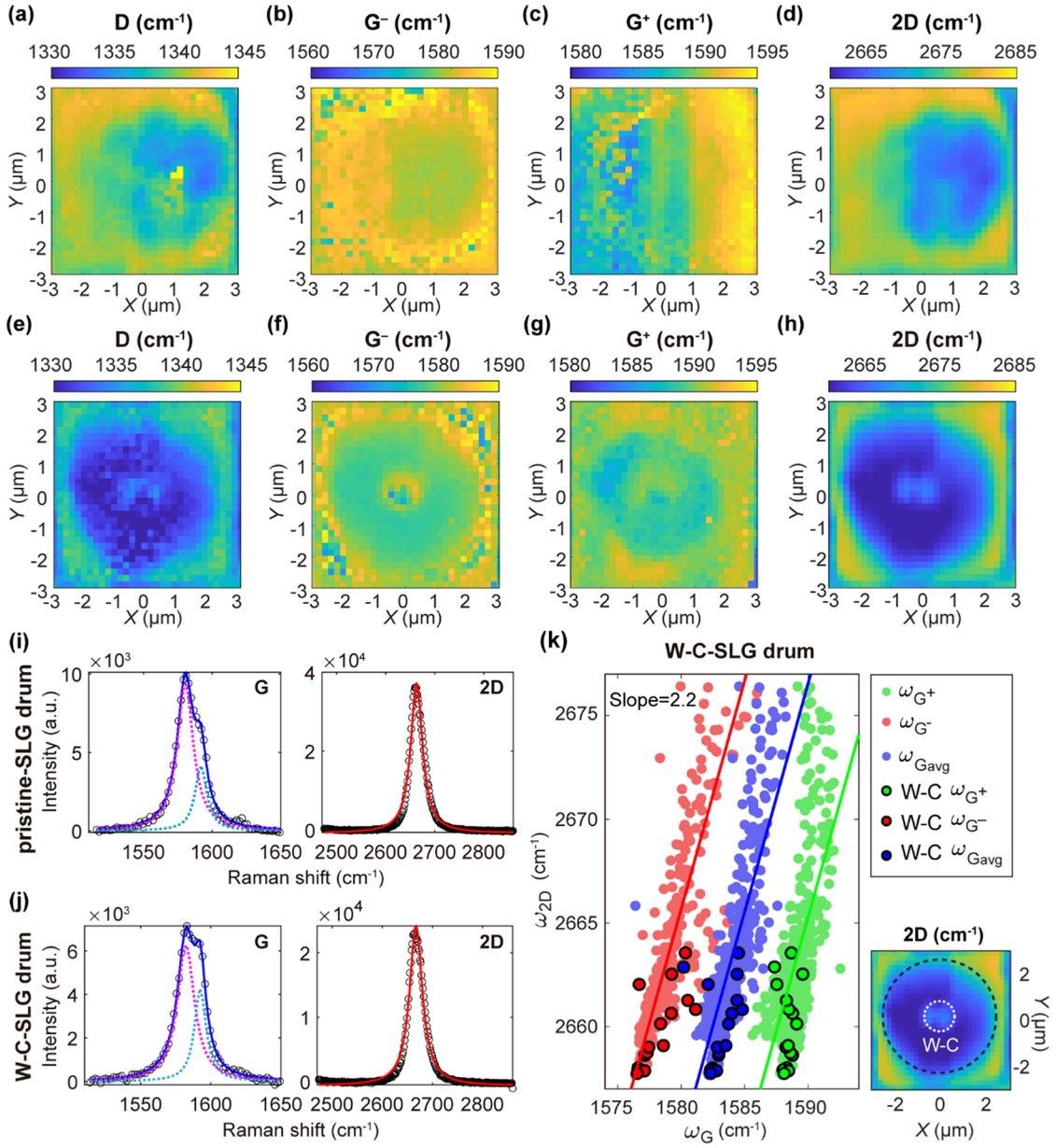


Figure 3. Raman spectral analysis of pristine-SLG and W−C−SLG drums. (a−d) Spatial maps of Raman peak positions for the pristine-SLG drum: (a) D band, (b) G^- band, (c) G^+ band, and (d) 2D band. (e−h) Corresponding maps for the W−C−SLG drum: (e) D, (f) G^-, (g) G^+, and (h) 2D band. (i, j) Representative Raman spectra acquired from each drum at the coordinate $(x, y) = (1.9, 0)$, along with the Lorentzian fitting results: (i) pristine-SLG drum, (j) W−C−SLG drum. The G band is fitted with two Lorentzian peaks corresponding to the G^- and G^+ components, while the 2D band is fitted with a single Lorentzian. (k) Correlation plot of the 2D peak position (ω_{2D}) versus the G peak position (ω_{G^+}, ω_{G^-}, $\omega_{G_{avg}}$) based on data from the W−C−SLG drum. Filled circles represent points in the undeposited region, while black-outlined symbols indicate data within the W−C deposition area. The extracted data points include G^+ frequency ω_{G^+}, G^- frequency ω_{G^-}, and the average G peak frequency $\omega_{G_{avg}} = (\omega_{G^+} + \omega_{G^-})/2$, plotted against the 2D peak frequency ω_{2D}. Both the W−C deposited and nondeposited regions are included in the correlation analysis. The linear fit yields a slope of approximately 2.2, indicating strain-dominant variations. The inset shows the 2D band map, identical to the data presented in panel h, with the W−C deposition area (white dashed line) and the data points (black dashed line) used for the correlation plot indicated by dashed outlines.

imentally observed mode at 49.6 MHz appears at a significantly higher frequency than expected for a fundamental mode (Figure 2f and Figure S3). COMSOL simulations using an effective phenomenological model suggest that the deposit-induced modification of the membrane mechanics can localize the fundamental-mode displacement near the center, thereby reducing its interferometric detectability through spatial averaging (Figure S4). Simultaneously, the deposit redistributes the pre-existing anisotropic in-plane tension into a more radially symmetric configuration, causing higher-order modes to develop a pronounced ring-like antinode around the deposit (Figure 2f inset) that is more readily detectable. Compared to the pristine-SLG drum, where the resonance mode reflects stronger stress along the x-direction, the W−C−SLG drum exhibits a more radially symmetric strain distribution. Similar behavior in a Pt−C−BLG drum (Figure S6) confirms that well-defined central deposition can override transfer-induced

https://doi.org/10.1021/acsami.5c25657
ACS Appl. Mater. Interfaces 2026, 18, 29208−29217

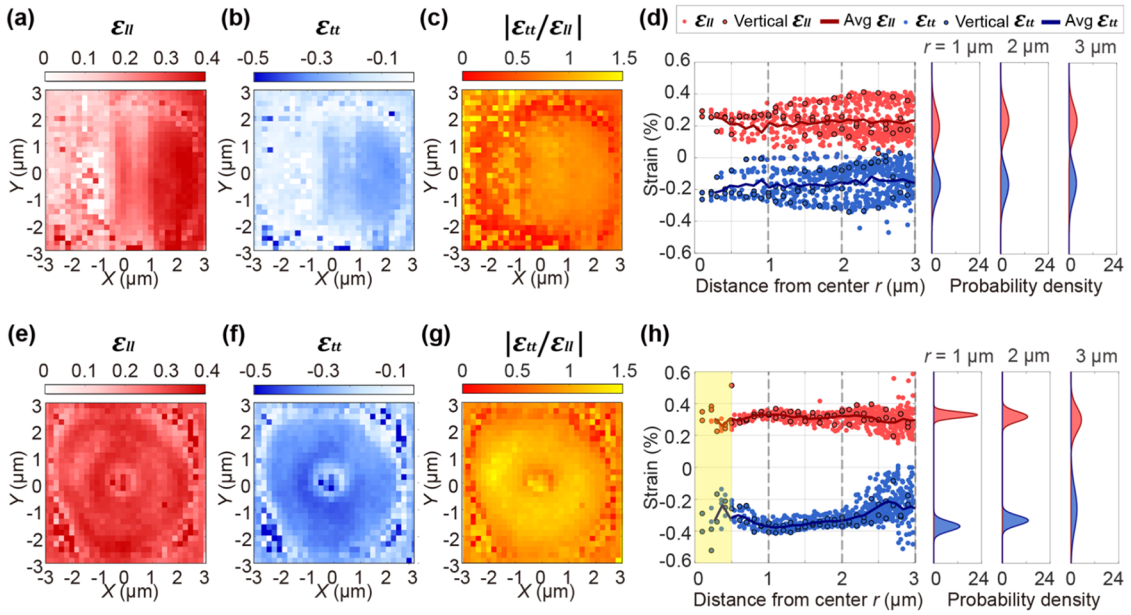


Figure 4. Strain maps and strain distribution as a function of distance from center for pristine-SLG and W−C−SLG drums based on Raman peak shifts. (a−e) Strain maps and distribution profile for the pristine-SLG drum: (a) longitudinal strain component (ε_{ll}), (b) transverse strain component (ε_{tt}), (c) Spatial maps of the absolute strain ratio $|\varepsilon_{tt}/\varepsilon_{ll}|$. (d) Strain distribution as a function of distance r from the center for pristine-SLG drum. Data points along vertical lines from the center to the edge of the square drum are marked with black outlines. Gaussian probability density plots on the right depict the distribution of ε_{ll} and ε_{tt} at r = 1, 2, and 3 μm. (e−g) Strain maps and distribution profile for the W−C−SLG drum: (e) Principal strain component (ε_{ll}), (f) Orthogonal principal strain component (ε_{tt}), (g) Spatial maps of the absolute strain ratio $|\varepsilon_{tt}/\varepsilon_{ll}|$. (h) Strain distribution as a function of distance r from the center for W−C−SLG drum. The yellow background highlights the region corresponding to the W−C deposit.

anisotropy and promote symmetric mode shapes regardless of deposit material.

Static Strain Fields from Spatial Raman Mapping

Spatial maps of the Raman peak positions for the D, G^-, and G^+, and 2D bands in pristine-SLG and W−C−SLG drums (Figure 3a−h) were obtained, with the corresponding intensity maps and raw Raman spectra shown in Figure S7. In the pristine-SLG drum, the D-band intensity shows slight spatial nonuniformity consistent with minor transfer-induced imperfections, while in the W−C−SLG drum a modest increase in background signal is observed near the W−C deposition center, with the G and 2D peaks remaining sharp and well-defined. In both samples, the G peak is clearly split into G^- and G^+ components, which are fitted with two Lorentzian functions, indicating the presence of anisotropic strain across the membrane. In contrast, the 2D peak is well described by single Lorentzian fits, as shown in representative Raman spectra from both samples measured at the same location (Figure 3i,j).

The Raman peak position maps for the pristine-SLG drum (Figure 3a−d) reveal spatial variations in the G^- and G^+ components, indicative of a nonuniform, asymmetrically biased strain distribution. This anisotropy is likely due to residual stress from the transfer process and is consistent with the distorted resonance modes in Figure 2c−e. In contrast, the W−C−SLG drum exhibits G^- and G^+ shifts that are radially symmetric around the W−C deposit (Figure 3e−h). While G peak splitting persists, indicating maintained anisotropy, the Raman data show that the strain field becomes more radially symmetric. This static symmetry aligns with the annular antinode observed in the dynamic measurements in Figure 2g.

To assess whether the observed Raman frequency shifts originated from mechanical strain or from charge doping associated with the W−C deposition, we performed a correlation analysis between the G and 2D peak positions in the W−C−SLG drum (Figure 3k). Data points were grouped into deposited regions (within 0.5 μm from the center, black-outlined circles) and nondeposited regions (within 2.5 μm, no outlines). The extracted slopes for ω_{G^+}, ω_{G^-}, and $\omega_{G_{avg}}$ were 2.27, 1.93, and 2.22, respectively, with an average of approximately 2.20 ± 0.15. This value is in close agreement with previously reported strain-dominated Raman shift ratios in graphene (≈2.2),[6,22,35−38] whereas charge doping typically yields significantly smaller slopes (≈0.75).[36,37] These results confirm that the observed spectral variations primarily arise from mechanical strain rather than doping effects. While we cannot entirely exclude minor doping effects from the deposition process, their contribution appears negligible compared with strain. We therefore attribute spatial variations in the Raman maps to strain redistribution rather than charge transfer.

From the Raman peak-position analysis, we derived strain maps and radial strain profiles for pristine-SLG (Figure 4a−c) and W−C−SLG drums (Figure 4e−g). The longitudinal (ε_{ll}) and transverse (ε_{tt}) strain components were obtained from the spatial variation in the G^+ and G^- peak positions (ω_{G^+} and ω_{G^-}) using the following expressions derived from the secular equation for the doubly degenerate E_{2g} phonon mode[8]

$$\varepsilon_{ll} = \frac{\Delta\omega_{G^+} + \Delta\omega_{G^-}}{4\omega_G^0\gamma_G} + \frac{\Delta\omega_{G+} - \Delta\omega_{G^-}}{2\omega_G^0\beta_G}$$

https://doi.org/10.1021/acsami.5c25657
ACS Appl. Mater. Interfaces 2026, 18, 29208−29217

$$\varepsilon_{tt} = \frac{\Delta\omega_{G^+} + \Delta\omega_{G^-}}{4\omega_G^0\gamma_G} - \frac{\Delta\omega_{G+} - \Delta\omega_{G^-}}{2\omega_G^0\beta_G}$$

where $\Delta\omega_{G^+}$ and $\Delta\omega_{G^-}$ denote the shifts of the G^+ and G^- peak positions relative to the reference G peak frequency ω_G^0. In the formal definition of the strain−Raman relation, ω_G^0 corresponds to the unstrained G-peak frequency. In our analysis, however, we used the G-peak frequency, ω_G^0 = 1584.67 cm^{-1}, measured from the exfoliated graphene on a SiO_2/Si substrate before transfer to the cavity (Figure 1b) as a practical experimental reference for evaluating relative frequency shifts upon suspension and subsequent deposition. To assess the sensitivity of the strain analysis to the choice of the reference frequency, we repeated the calculation using a commonly reported literature value of ω_G^0 = 1580 cm^{-1} for monolayer graphene in the Supporting Information (Figure S8).[39] Although the absolute strain magnitudes change, as expected, the overall spatial distribution and the qualitative trends of the strain field remain unchanged. The Grüneisen parameter γ_G = 1.99 and shear deformation potential β_G = 0.99 were adopted from ref 11. Here, ε_{ll} and ε_{tt} represent the two local principal strain components obtained from the G-band splitting, rather than fixed components in a single global coordinate system. In the pristine-SLG drum, these directions are approximately aligned with the x- and y-axes, whereas in the W−C−SLG drum they vary spatially and are better described by local radial and circumferential directions.

In the pristine-SLG drum, ε_{ll} shows strongly anisotropic tensile strain with a high-strain zone between x = 1 μm and x = 3 μm (Figure 4a), while ε_{tt} exhibits the corresponding orthogonal Raman-derived component (Figure 4b), consistent with the anisotropic response expected for a Poisson-type response.[40] In contrast, W−C−SLG displays radially symmetric distributions in both strain components (Figure 4e,g), indicating that the central deposit redistributes the pre-existing anisotropic strain state into a strain field with reduced angular variation.

The degree of anisotropy was quantified via the absolute strain ratio $|\varepsilon_{tt}/\varepsilon_{ll}|$ (Figure 4c,4g). The pristine-SLG drum yields an average ratio of 0.69, while W−C−SLG reaches 0.93, indicating that the two Raman-derived principal components approach similar magnitudes. Both strain components increase in magnitude, consistent with the radial wrinkles observed in the SEM image (Figure S9).

To quantify the angular variation of the strain field, we analyzed the angular dependence of the strain components. Figure 4d,h show the radial profiles of ε_{ll} and ε_{tt} as a function of radial distance r from the drum center, with solid lines indicating the angular averages (μ). At each radial position, the angular standard deviation (σ) was calculated and then averaged over the entire radius.

The pristine-SLG drum shows spatial asymmetry with larger fluctuations ($\sigma_{\varepsilon_{ll}}$ = 0.10%, $\sigma_{\varepsilon_{tt}}$ = 0.10%), whereas the W−C−SLG drum exhibits reduced angular variation in the strain field ($\sigma_{\varepsilon_{ll}}$ = 0.046%, $\sigma_{\varepsilon_{tt}}$ = 0.09%). Moreover, the W−C−SLG drum displays higher average magnitudes ($\mu_{\varepsilon_{ll}}$ = 0.31%, $\mu_{\varepsilon_{tt}}$ = −0.30%) compared to the pristine sample ($\mu_{\varepsilon_{ll}}$ = 0.22%, $\mu_{\varepsilon_{tt}}$ = −0.16%). Gaussian probability density plots at r = 1 μm highlight these differences: W−C−SLG shows sharply peaked, narrow distributions ($\mu_{\varepsilon_{ll}}$ = 0.33%, $\sigma_{\varepsilon_{ll}}$ = 0.02%; $\mu_{\varepsilon_{tt}}$ = −0.37%, $\sigma_{\varepsilon_{tt}}$ = 0.03%) compared to the broader, flatter peaks in the pristine drum ($\mu_{\varepsilon_{ll}}$ = 0.20%, $\sigma_{\varepsilon_{ll}}$ = 0.10%; $\mu_{\varepsilon_{tt}}$ = −0.17%, $\sigma_{\varepsilon_{tt}}$ = 0.09%). The smaller σ values indicate suppressed local strain fluctuations and a more homogeneous strain distribution in the W−C−SLG drum. Note that a negative ε_{tt} should not be interpreted simply as a large stored in-plane compressive strain in a suspended membrane region, because compressive components can be partially relaxed through out-of-plane wrinkling or buckling.[41] Therefore, in the present study, the spatial homogeneity of the Raman-derived strain components is more physically meaningful than their absolute magnitudes.

Our static strain maps clearly show that the strain field is radially redistributed, indicating that the W−C deposit is mechanically coupled to the graphene. This coupling likely originates from a combination of interfacial bonding and material modification induced during FEBID, together with the added mass of the deposited feature. The W−C deposit contains a significant amount of amorphous carbon[42−44] and is formed under high-energy electron beam irradiation, which can locally alter the atomic structure of graphene. The irradiation can also induce defect formation and changes in bonding configurations,[45] such as sp^2-to-sp^3 transitions.[46] These effects may alter the interfacial mechanical coupling between the graphene and the deposit, locally modifying the membrane's mechanical properties and inducing radial stress redistribution. In addition to interfacial mechanical modification, intrinsic stress within the deposited material and thermomechanical effects arising from localized e-beam heating are also expected to contribute, so that several mechanisms act concurrently to reshape the membrane's intrinsic tension. Disentangling their relative influence will require systematic studies that integrate in situ mechanical probing with complementary spectroscopic and high-resolution structural characterization. The observed effects are not specific to the W−C material system but arise from the localized mechanical perturbation introduced by the deposited nanostructure. Similar qualitative trends may therefore occur for other FEBID materials.

Furthermore, although the Raman-derived strain maps and the observed resonance-mode evolution are qualitatively consistent, establishing a direct quantitative correspondence between the two remains challenging. The Raman measurements provide local principal strain information extracted from the G^+/G^- splitting, but do not directly yield a complete boundary-condition-ready stress tensor field that can be uniquely implemented in the FEM model. In addition, the present COMSOL framework does not readily allow a point-by-point import of experimentally measured strain maps in a mechanically self-consistent manner. Therefore, the FEM analysis presented here should be understood as a simplified mechanical model that captures the overall stress redistribution trend rather than a unique quantitative reconstruction of the Raman-derived strain field.

A broader implication of our findings is that FEBID provides a lithography-free, site-specific route to introduce a localized central perturbation in suspended graphene membranes after fabrication. In the devices studied here, the W−C deposit acts not only as a local proof mass that can exceed the membrane's own mass by more than an order of magnitude, but also as a mechanically coupled feature that redistributes the pre-existing membrane stress into a more radially symmetric configuration. These results establish FEBID as a practical experimental platform for studying the mechanical consequences of localized central perturbations in suspended 2D membranes. Such

https://doi.org/10.1021/acsami.5c25657
ACS Appl. Mater. Interfaces 2026, 18, 29208−29217

localized postfabrication modification of mass and membrane stress is relevant to the design of NEMS architectures that rely on controlled proof masses, including 2D-material-based accelerometers and gyroscopes.[47−49] Compared to conventional SOI-based multilayer processes used to suspend large silicon proof masses on graphene membranes,[47,48] FEBID offers a highly localized, mask-free route for postfabrication adjustment of the mechanical properties. We therefore expect that the platform established here will provide a practical experimental framework for studies of strain-coupled phenomena and for future optomechanical systems and strain- and mass-engineered 2D NEMS.

CONCLUSIONS

We demonstrated that localized deposition via FEBID effectively modulates the strain distribution in suspended monolayer graphene membranes. Central deposition acts as a mechanically coupled local perturbation that redistributes the pre-existing, transfer-induced strain from a spatially nonuniform state into a strain configuration with enhanced radial symmetry and reduced angular variation. Optical interferometry-based resonance mode mapping and finite element simulations revealed this transition from asymmetric to radially symmetric stress profiles. Raman spectroscopy confirmed the redistribution, showing the G-peak splitting into G^- and G^+ components with enhanced tensile strain. Importantly, while the strain becomes more radially symmetric with reduced angular variation, it remains anisotropic with radial tension and a negative circumferential Raman-derived strain component. These findings establish FEBID as a lithography-free approach to locally modulate strain in suspended 2D membranes without altering boundary conditions. Unlike global deformation methods, localized deposition enables site-specific strain engineering while maintaining membrane geometry. This approach complements existing global and highly localized strain control techniques, providing an experimental platform for strain-engineered devices and exploration of strain-coupled phenomena in two-dimensional materials. Establishing a quantitative link between Raman-derived strain tensors and dynamic resonance behavior remains an open challenge and will require future studies combining higher-resolution strain mapping with experimentally constrained mechanical modeling.

METHODS

Square Graphene Drum Fabrication

The square graphene drum resonators were prepared by transferring exfoliated monolayer graphene onto silicon substrates patterned with square-shaped trenches. Details of the fabrication process are described in the Supporting Information Figure S12. The pristine-SLG drum was prepared without FEBID, whereas the W−C−SLG drum was specifically fabricated with a tungsten carbide (W−C) structure deposited in the center of the drum. In these devices, the graphene square drums were clamped using cross-linked PMMA bars. The gold electrode on the trench substrate, used to contact the graphene, was fabricated with photolithography, followed by the sequential deposition via e-beam evaporation of 10 nm chromium and 60 nm gold layers onto the 300 nm SiO_2/p-doped silicon substrate. To fabricate square-shaped trenches, two layers of poly(methyl methacrylate) (PMMA) (C4) and one layer of SML 300 were spin-coated in sequence onto the SiO_2/Si substrate with the prefabricated electrodes. These layers were then patterned with the desired trench configuration. After the development of the patterns, the SiO_2 layer within the trench area was selectively etched using reactive ion etching (CF_4) and the e-beam resist was removed using chloroform. The resulting square trenches possess approximate dimensions of 280 nm in depth and 7 μm in length. Mechanically exfoliated monolayer graphene was then transferred onto the patterned substrate using a PMMA wet transfer method. To clamp the graphene, the PMMA surrounding the trench was cross-linked through exposure to an excess dose of electron-beam radiation (area dose 8000 mAs/cm^2, beam current 200 pA). Finally, to prevent the collapse of the suspended graphene, the graphene square resonator was subjected to critical point drying following the removal of non-cross-linked PMMA.

Focused Electron Beam Induced Deposition (FEBID) Process

Following the preparation of the suspended graphene square drum resonators, a W−C structure was precisely deposited onto the graphene surface using FEBID. To achieve this, the deposition was carried out using a Thermo Fisher Helios G4 CX DualBeam system equipped with a Gas Injection System (GIS) and a $W(CO)_6$ metal−organic precursor. The FEBID was conducted using a primary beam energy of 10 keV and a beam current of 0.69 nA. Under these beam conditions, $W(CO)_6$-based FEBID enabled stable and reproducible nanostructure deposition on suspended monolayer graphene. First, a precursor gas was introduced into the chamber, ensuring that the sample was enveloped in a reactive environment. Then, a focused electron beam scanned the sample, following a defined geometric pattern. This induced the breakdown of the precursor molecules into a nonvolatile part that adhered to the substrate and a volatile part that is removed. As reported previously, FEBID deposits created from $W(CO)_6$ are not composed of pure metallic tungsten, but typically consist of oxidized tungsten atoms embedded in a diamond-like amorphous carbon matrix.[31,50−52] The purity of tungsten in as-deposited nanostructures is typically limited to approximately 60% based on EDX analysis.[52−55] The deposition process was controlled to ensure accurate positioning, and the W−C structure was centrally aligned on the graphene drum to maintain a symmetrical mass distribution.[56] SEM images were used to confirm the successful deposition of the W−C structure on the graphene surface. In addition to the W−C-deposited samples, bilayer graphene square drums were fabricated following a similar procedure. A Pt−C nanostructure was deposited at the center of one drum using the same FEBID method with a $MeCpPtMe_3$ precursor. Further FEBID process for Pt−C deposition on bilayer graphene drums can be found in the Supporting Information S1.

Resonance Frequency and Mode Measurement

Mechanical resonance frequencies were measured at room temperature in a vacuum environment (~10^{-5} Torr) using an optical interferometry setup. This system includes a photodetector (Menlo systems FPD510-FV), a 633 nm He−Ne laser, a lock-in amplifier (Zurich instrument UHFLI), a function generator (Tektronix AFG-3102), and a motorized *x-y* nanopositioning stage (Newport NPXYZ100SGV6). The graphene resonators were actuated by an electrostatic force applied between the graphene membrane and Si substrate. AC signals were applied to the electrode contacting the suspended graphene. The graphene resonator exhibits oscillations when the applied AC frequency matches a mechanical resonance frequency of the membrane. To characterize the mechanical resonance modes of the graphene drum resonators, spatially resolved vibration amplitude measurements were conducted using a motorized *x-y* nanopositioning stage located beneath the sample. The stage was programmed using LabVIEW to scan the sample surface with submicrometer step sizes, allowing the laser beam to sequentially probe different positions on the suspended membrane. At each point, the out-of-plane vibration amplitude was recorded using an optical interferometric detection system. By assembling these point-by-point measurements, a high-resolution spatial map of the vibrational mode shape was reconstructed, enabling precise identification of nodal lines and antinodes in the resonator.

https://doi.org/10.1021/acsami.5c25657
ACS Appl. Mater. Interfaces 2026, 18, 29208−29217

Spatially Resolved Raman Spectroscopy

Raman spectroscopy mapping was performed to quantitatively analyze the spatial strain distribution in the suspended graphene membranes. A confocal Raman microscope system (Nanobase) with a 532 nm excitation laser was employed, with the beam focused onto the sample via a 40× objective lens. The laser spot was scanned across the suspended membrane using a galvo mirror system, enabling 2D mapping without moving the sample stage. The backscattered Raman signal was collected and passed through a long-pass filter (LPF), then focused onto a confocal pinhole placed in front of the spectrometer to reject out-of-focus light. The filtered signal was subsequently guided into the spectrometer equipped with a CCD detector for spectral acquisition. Raman spectra were acquired with a scan step size of 200 nm in both x and y directions and an exposure time of 16 s per spectrum, ensuring high spatial resolution. The acquired spectra were processed to extract the positions of the D, G^+, G^-, and 2D peaks, which were subsequently used to compute strain maps and strain profiles across the suspended graphene drums.

■ ASSOCIATED CONTENT

Supporting Information

The Supporting Information is available free of charge at https://pubs.acs.org/doi/10.1021/acsami.5c25657.

Bilayer graphene (BLG) square drum resonators with and without Pt−C deposition; mechanical resonance frequency and mode observations of pristine-BLG and Pt−C−BLG drums; spatial Raman intensity maps and representative raw spectra of pristine-SLG and W−C−SLG drums; SEM images showing wrinkle formation around the central deposit; schematic illustration of the graphene square drum fabrication process; time stability of resonance frequency and vibrational mode shapes; strain maps from multiple samples with varying layer numbers and deposit geometries; finite-element simulations of mass loading, Young's modulus variation, and central compressive force in graphene membranes; raw resonance spectra of W−C−SLG drum measured by optical interferometry; and analysis of the influence of the reference G-peak frequency on the extracted strain components (PDF)

■ AUTHOR INFORMATION

Corresponding Authors

Sang Wook Lee − *Department of Physics, Ewha Womans University, Seoul 03760, Republic of Korea; Institute for Multiscale Matter and Systems, Ewha Womans University, Seoul 03760, Republic of Korea;* orcid.org/0000-0003-2265-4761; Email: leesw@ewha.ac.kr

Dong Hoon Shin − *Department of Electronics and Information Engineering, Korea University, Sejong 30019, Republic of Korea*; Email: shindh@korea.ac.kr

Authors

Yugyeong Je − *Department of Physics, Ewha Womans University, Seoul 03760, Republic of Korea;* orcid.org/0009-0003-8856-3552

Hyunjeong Jeong − *Department of Physics, Ewha Womans University, Seoul 03760, Republic of Korea*

Sabina Caneva − *Department of Precision and Microsystems Engineering, Delft University of Technology, 2628 CD Delft, The Netherlands;* orcid.org/0000-0003-3457-7505

Peter G. Steeneken − *Department of Precision and Microsystems Engineering, Delft University of Technology, 2628 CD Delft, The Netherlands;* orcid.org/0000-0002-5764-1218

Eleanor E. B. Campbell − *School of Chemistry, University of Edinburgh, Edinburgh, Scotland, United Kingdom;* orcid.org/0000-0002-4656-3218

Complete contact information is available at: https://pubs.acs.org/10.1021/acsami.5c25657

Author Contributions

#Y.J. and H.J. contributed equally to this work.

Notes

The authors declare no competing financial interest.

■ ACKNOWLEDGMENTS

This research was supported by National Research Foundation of Korea (NRF) grant funded by the Korean government (MSIT and MOE) (No. RS-2025-16063688), by Basic Research Program (NRF-2021R1A6A1A10039823, RS-2026-25485403) through the National Research Foundation of Korea (NRF), and by IITP (Institute of Information & Communications Technology Planning & Evaluation)-ITRC (Information Technology Research Center) (IITP-2025-RS-2024-00437191) grant funded by the Korea government (Ministry of Science and ICT). D.H.S. was supported by a Korea University Grant, by the Alchemist Project grant funded by Korea Planning & Evaluation Institute of Industrial Technology (KEIT) & the Korea Government (MOTIE) (Project Number: 1415185027, 20019169), and by the Regional Innovation System & Education (RISE) program through the Sejong RISE Center, funded by the Ministry of Education (MOE) and the Sejong City, Republic of Korea (2025-RISE-08-001). S.C. was supported by an ERC starting grant (SIMPHONICS, No. 101041486) and a Delft Technology Fellowship. P.G.S. acknowledges funding by the European Union's Horizon Europe Coordination and Support Programme, Grant Agreement No: 101136388 (TEAM-NANO project).

■ REFERENCES

(1) Dai, Z.; Liu, L.; Zhang, Z. Strain engineering of 2D materials: issues and opportunities at the interface. *Adv. Mater.* **2019**, *31* (45), No. 1805417.

(2) Qi, Y.; Sadi, M. A.; Hu, D.; Zheng, M.; Wu, Z.; Jiang, Y.; Chen, Y. P. Recent progress in strain engineering on van der Waals 2D materials: Tunable electrical, electrochemical, magnetic, and optical properties. *Adv. Mater.* **2023**, *35* (12), No. 2205714.

(3) Chaves, A.; Azadani, J. G.; Alsalman, H.; Da Costa, D.; Frisenda, R.; Chaves, A.; Song, S. H.; Kim, Y. D.; He, D.; Zhou, J.; et al. Bandgap engineering of two-dimensional semiconductor materials. *npj 2D Mater. Appl.* **2020**, *4* (1), No. 29.

(4) Di Giorgio, C.; Blundo, E.; Pettinari, G.; Felici, M.; Bobba, F.; Polimeni, A. Mechanical, Elastic, and Adhesive Properties of Two-Dimensional Materials: From Straining Techniques to State-of-the-Art Local Probe Measurements. *Adv. Mater. Interfaces* **2022**, *9* (13), No. 2102220.

(5) Guan, F.; Kumaravadivel, P.; Averin, D. V.; Du, X. Tuning strain in flexible graphene nanoelectromechanical resonators. *Appl. Phys. Lett.* **2015**, *107* (19), No. 193102, DOI: 10.1063/1.4935239.

(6) Zhang, X.; Makles, K.; Colombier, L.; Metten, D.; Majjad, H.; Verlot, P.; Berciaud, S. Dynamically-enhanced strain in atomically thin resonators. *Nat. Commun.* **2020**, *11* (1), No. 5526.

(7) Lindahl, N.; Midtvedt, D.; Svensson, J.; Nerushev, O. A.; Lindvall, N.; Isacsson, A.; Campbell, E. E. B. Determination of the

bending rigidity of graphene via electrostatic actuation of buckled membranes. *Nano Lett.* **2012**, *12* (7), 3526−3531.
(8) Mohiuddin, T.; Lombardo, A.; Nair, R.; Bonetti, A.; Savini, G.; Jalil, R.; Bonini, N.; Basko, D.; Galiotis, C.; Marzari, N.; et al. Uniaxial strain in graphene by Raman spectroscopy: G peak splitting, Grüneisen parameters, and sample orientation. *Phys. Rev. B* **2009**, *79* (20), No. 205433.
(9) Androulidakis, C.; Koukaras, E. N.; Parthenios, J.; Kalosakas, G.; Papagelis, K.; Galiotis, C. Graphene flakes under controlled biaxial deformation. *Sci. Rep.* **2016**, *5* (1), No. 18219.
(10) Gao, X.; Sun, H.; Kang, D.-H.; Wang, C.; Wang, Q. J.; Nam, D. Heterostrain-enabled dynamically tunable moiré superlattice in twisted bilayer graphene. *Sci. Rep.* **2021**, *11* (1), No. 21402.
(11) Jiang, T.; Wang, Z.; Ruan, X.; Zhu, Y. Equi-biaxial compressive strain in graphene: Grüneisen parameter and buckling ridges. *2D Mater.* **2019**, *6* (1), No. 015026.
(12) Gablech, I.; Brodský, J.; Vyroubal, P.; Piastek, J.; Bartošík, M.; Pekárek, J. Mechanical strain and electric-field modulation of graphene transistors integrated on MEMS cantilevers. *J. Mater. Sci.* **2022**, *57* (3), 1923−1935.
(13) Li, X.; Zhang, R.; Yu, W.; Wang, K.; Wei, J.; Wu, D.; Cao, A.; Li, Z.; Cheng, Y.; Zheng, Q.; et al. Stretchable and highly sensitive graphene-on-polymer strain sensors. *Sci. Rep.* **2012**, *2* (1), No. 870.
(14) Anagnostopoulos, G.; Androulidakis, C.; Koukaras, E. N.; Tsoukleri, G.; Polyzos, I.; Parthenios, J.; Papagelis, K.; Galiotis, C. Stress transfer mechanisms at the submicron level for graphene/polymer systems. *ACS Appl. Mater. Interfaces* **2015**, *7* (7), 4216−4223.
(15) Li, Z.; Lv, Y.; Ren, L.; Li, J.; Kong, L.; Zeng, Y.; Tao, Q.; Wu, R.; Ma, H.; Zhao, B.; et al. Efficient strain modulation of 2D materials via polymer encapsulation. *Nat. Commun.* **2020**, *11* (1), No. 1151.
(16) Peng, Z.; Chen, X.; Fan, Y.; Srolovitz, D. J.; Lei, D. Strain engineering of 2D semiconductors and graphene: from strain fields to band-structure tuning and photonic applications. *Light:Sci. Appl.* **2020**, *9* (1), No. 190.
(17) Hsu, C.-C.; Teague, M.; Wang, J.-Q.; Yeh, N.-C. Nanoscale strain engineering of giant pseudo-magnetic fields, valley polarization, and topological channels in graphene. *Sci. Adv.* **2020**, *6* (19), No. eaat9488.
(18) Yang, H. T. Strain induced shift of Dirac points and the pseudo-magnetic field in graphene. *J. Phys.: Condens. Matter* **2011**, *23* (50), No. 505502.
(19) Klimov, N. N.; Jung, S.; Zhu, S.; Li, T.; Wright, C. A.; Solares, S. D.; Newell, D. B.; Zhitenev, N. B.; Stroscio, J. A. Electromechanical properties of graphene drumheads. *Science* **2012**, *336* (6088), 1557−1561.
(20) Settnes, M.; Power, S. R.; Brandbyge, M.; Jauho, A.-P. Graphene nanobubbles as valley filters and beam splitters. *Phys. Rev. Lett.* **2016**, *117* (27), No. 276801.
(21) Levy, N.; Burke, S.; Meaker, K.; Panlasigui, M.; Zettl, A.; Guinea, F.; Neto, A. C.; Crommie, M. F. Strain-induced pseudo−magnetic fields greater than 300 T in graphene nanobubbles. *Science* **2010**, *329* (5991), 544−547.
(22) Elibol, K.; Bayer, B. C.; Hummel, S.; Kotakoski, J.; Argentero, G.; Meyer, J. C. Visualising the strain distribution in suspended two-dimensional materials under local deformation. *Sci. Rep.* **2016**, *6* (1), No. 28485.
(23) Lee, C.; Wei, X.; Kysar, J. W.; Hone, J. Measurement of the elastic properties and intrinsic strength of monolayer graphene. *Science* **2008**, *321* (5887), 385−388.
(24) Li, H.; Contryman, A. W.; Qian, X.; Ardakani, S. M.; Gong, Y.; Wang, X.; Weisse, J. M.; Lee, C. H.; Zhao, J.; Ajayan, P. M.; et al. Optoelectronic crystal of artificial atoms in strain-textured molybdenum disulphide. *Nat. Commun.* **2015**, *6* (1), No. 7381.
(25) Tomori, H.; Kanda, A.; Goto, H.; Ootuka, Y.; Tsukagoshi, K.; Moriyama, S.; Watanabe, E.; Tsuya, D. Introducing nonuniform strain to graphene using dielectric nanopillars. *Appl. Phys. Express* **2011**, *4* (7), No. 075102.
(26) Neek-Amal, M.; Covaci, L.; Peeters, F. Nanoengineered nonuniform strain in graphene using nanopillars. *Phys. Rev. B* **2012**, *86* (4), No. 041405.
(27) Chaste, J.; Missaoui, A.; Huang, S.; Henck, H.; Ben Aziza, Z.; Ferlazzo, L.; Naylor, C.; Balan, A.; Johnson, A. T. C., Jr; Braive, R.; Ouerghi, A. Intrinsic properties of suspended MoS2 on SiO2/Si pillar arrays for nanomechanics and optics. *ACS Nano* **2018**, *12* (4), 3235−3242.
(28) Davidovikj, D.; Slim, J. J.; Cartamil-Bueno, S. J.; van der Zant, H. S.; Steeneken, P. G.; Venstra, W. J. Visualizing the Motion of Graphene Nanodrums. *Nano Lett.* **2016**, *16* (4), 2768−2773.
(29) Sarafraz, A.; Liu, H.; Cvetanović, K.; Spasenović, M.; Vollebregt, S.; Garcia, T. M.; Steeneken, P. G.; Alijani, F.; Verbiest, G. J. Quantifying stress distribution in ultra-large graphene drums through mode shape imaging. *npj 2D Mater. Appl.* **2024**, *8* (1), No. 45.
(30) Mulders, J. J. L.; Belova, L.; Riazanova, A. Electron beam induced deposition at elevated temperatures: compositional changes and purity improvement. *Nanotechnology* **2011**, *22* (5), No. 055302.
(31) Rosenberg, S. G.; Barclay, M.; Fairbrother, D. H. Electron induced reactions of surface adsorbed tungsten hexacarbonyl (W (CO) 6). *Phys. Chem. Chem. Phys.* **2013**, *15* (11), 4002−4015.
(32) Yu, Y.-J.; Zhao, Y.; Ryu, S.; Brus, L. E.; Kim, K. S.; Kim, P. Tuning the graphene work function by electric field effect. *Nano Lett.* **2009**, *9* (10), 3430−3434.
(33) Khomyakov, P. A.; Giovannetti, G.; Rusu, P.; Brocks, Gv.; Van den Brink, J.; Kelly, P. J. First-principles study of the interaction and charge transfer between graphene and metals. *Phys. Rev. B* **2009**, *79* (19), No. 195425.
(34) Giovannetti, G.; Khomyakov, P. A.; Brocks, G.; Karpan, Vv.; van den Brink, J.; Kelly, P. J. Doping graphene with metal contacts. *Phys. Rev. Lett.* **2008**, *101* (2), No. 026803.
(35) Mueller, N. S.; Heeg, S.; Alvarez, M. P.; Kusch, P.; Wasserroth, S.; Clark, N.; Schedin, F.; Parthenios, J.; Papagelis, K.; Galiotis, C.; et al. Evaluating arbitrary strain configurations and doping in graphene with Raman spectroscopy. *2D Mater.* **2018**, *5* (1), No. 015016.
(36) Lee, T.; Mas' ud, F. A.; Kim, M. J.; Rho, H. Spatially resolved Raman spectroscopy of defects, strains, and strain fluctuations in domain structures of monolayer graphene. *Sci. Rep.* **2017**, *7* (1), No. 16681.
(37) Lee, J. E.; Ahn, G.; Shim, J.; Lee, Y. S.; Ryu, S. Optical separation of mechanical strain from charge doping in graphene. *Nat. Commun.* **2012**, *3* (1), No. 1024.
(38) Metten, D.; Federspiel, F.; Romeo, M.; Berciaud, S. All-optical blister test of suspended graphene using micro-Raman spectroscopy. *Phys. Rev. Appl.* **2014**, *2* (5), No. 054008.
(39) Ferrari, A. C.; Meyer, J. C.; Scardaci, V.; Casiraghi, C.; Lazzeri, M.; Mauri, F.; Piscanec, S.; Jiang, D.; Novoselov, K. S.; Roth, S.; Geim, A. K. Raman spectrum of graphene and graphene layers. *Phys. Rev. Lett.* **2006**, *97* (18), No. 187401.
(40) Shioya, H.; Craciun, M. F.; Russo, S.; Yamamoto, M.; Tarucha, S. Straining graphene using thin film shrinkage methods. *Nano Lett.* **2014**, *14* (3), 1158−1163.
(41) Polyzos, I.; Bianchi, M.; Rizzi, L.; Koukaras, E. N.; Parthenios, J.; Papagelis, K.; Sordan, R.; Galiotis, C. Suspended monolayer graphene under true uniaxial deformation. *Nanoscale* **2015**, *7* (30), 13033−13042.
(42) Sullivan, J.; Friedmann, T.; Baca, A. Stress relaxation and thermal evolution of film properties in amorphous carbon. *J. Electron. Mater.* **1997**, *26*, 1021−1029.
(43) Charitidis, C.; Logothetidis, S.; Douka, P. Nanoindentation and nanoscratching studies of amorphous carbon films. *Diamond Relat. Mater.* **1999**, *8* (2−5), 558−562.
(44) Ong, S.-E.; Zhang, S.; Du, H.; Sun, D. Relationship between bonding structure and mechanical properties of amorphous carbon containing silicon. *Diamond Relat. Mater.* **2007**, *16* (8), 1628−1635.
(45) Murakami, K.; Kadowaki, T.; Fujita, J.-i. Damage and strain in single-layer graphene induced by very-low-energy electron-beam

https://doi.org/10.1021/acsami.5c25657
ACS Appl. Mater. Interfaces 2026, 18, 29208−29217

irradiation. *Appl. Phys. Lett.* **2013**, *102* (4), No. 043111, DOI: 10.1063/1.4790388.
(46) Kim, S.; Kulkarni, D. D.; Davis, R.; Kim, S. S.; Naik, R. R.; Voevodin, A. A.; Russell, M.; Jang, S. S.; Tsukruk, V. V.; Fedorov, A. G. Controlling the physicochemical state of carbon on graphene using focused electron-beam-induced deposition. *ACS Nano* **2014**, *8* (7), 6805−6813.
(47) Fan, X.; Forsberg, F.; Smith, A. D.; Schröder, S.; Wagner, S.; Rödjegård, H.; Fischer, A. C.; Östling, M.; Lemme, M. C.; Niklaus, F. Graphene ribbons with suspended masses as transducers in ultra-small nanoelectromechanical accelerometers. *Nat. Electron.* **2019**, *2* (9), 394−404.
(48) Fan, X.; Smith, A. D.; Forsberg, F.; Wagner, S.; Schröder, S.; Akbari, S. S. A.; Fischer, A. C.; Villanueva, L. G.; Östling, M.; Lemme, M. C.; Niklaus, F. Manufacture and characterization of graphene membranes with suspended silicon proof masses for MEMS and NEMS applications. *Microsyst. Nanoeng.* **2020**, *6* (1), No. 17.
(49) Hurst, A. M.; Lee, S.; Cha, W.; Hone, J. In *A graphene accelerometer*, 2015 28th IEEE International Conference on Micro Electro Mechanical Systems (MEMS); IEEE, 2015; pp 865−868.
(50) Haub, M.; Günther, T.; Bogner, M.; Zimmermann, A. Investigation of focused ion and electron beam platinum carbon nano-tips with transmission electron microscopy for quantum tunneling vacuum gap applications. *Appl. Sci.* **2021**, *11* (24), No. 11793.
(51) Kometani, R.; Ichihashi, T.; Kanda, K.; Suzuki, T.; Niihara, K.; Ishihara, S.; Kaito, T.; Matsui, S. Resistivity change of the diamondlike carbon, deposited by focused-ion-beam chemical vapor deposition, induced by the annealing treatment. *J. Vac. Sci. Technol., B:Microelectron. Nanometer Struct.–Process., Meas., Phenom.* **2008**, *26* (6), 2628−2631.
(52) Henry, M. R.; Kim, S.; Fedorov, A. G. High purity tungsten nanostructures via focused electron beam induced deposition with carrier gas assisted supersonic jet delivery of organometallic precursors. *J. Phys. Chem. C* **2016**, *120* (19), 10584−10590.
(53) Koops, H. W. P.; Weiel, R.; Kern, D.; Baum, T. High-resolution electron-beam induced deposition. *J. Vac. Sci. Technol., B:Microelectron. Process. Phenom.* **1988**, *6* (1), 477−481.
(54) Hoyle, P. C.; Cleaver, J.; Ahmed, H. Electron beam induced deposition from W (CO) 6 at 2 to 20 keV and its applications. *J. Vac. Sci. Technol., B:Microelectron. Nanometer Struct.–Process., Meas., Phenom.* **1996**, *14* (2), 662−673.
(55) Botman, A.; Mulders, J.; Hagen, C. Creating pure nanostructures from electron-beam-induced deposition using purificationtechniques: a technology perspective. *Nanotechnology* **2009**, *20* (37), No. 372001.
(56) Ramos, D.; Tamayo, J.; Mertens, J.; Calleja, M.; Zaballos, A. Origin of the response of nanomechanical resonators to bacteria adsorption. *J. Appl. Phys.* **2006**, *100* (10), 1−3, DOI: 10.1063/1.2370507.



https://doi.org/10.1021/acsami.5c25657
ACS Appl. Mater. Interfaces 2026, 18, 29208−29217